Effect of single-step hot isostatic pressing & solution treatment on the microstructure of Al-Cu-Mg-Ag-Ti-B (A205) alloy processed by laser powder bed fusion

Original
Effect of single-step hot isostatic pressing & solution treatment on the microstructure of Al-Cu-Mg-Ag-Ti-B (A205) alloy processed by laser powder bed fusion / Barode, J., Bassini, E., Aversa, A., D'Isanto, F., Ugues, D., Biamino, S., Lombardi, M., Fino, P.. - In: JOURNAL OF ALLOYS AND COMPOUNDS. - ISSN 0925-8388. - 1036:(2025). [10.1016/j.jallcom.2025.181817]

Publisher:
Elsevier

Published
DOI:10.1016/j.jallcom.2025.181817

Journal of Alloys and Compounds 1036 (2025) 181817

Contents lists available at ScienceDirect

Journal of Alloys and Compounds

journal homepage: www.elsevier.com/locate/jalcom

Effect of single-step hot isostatic pressing & solution treatment on the microstructure of Al-Cu-Mg-Ag-Ti-B (A205) alloy processed by laser powder bed fusion

J. Barode [a], E. Bassini [a,*], A. Aversa [a,b], F. D'Isanto [a,b], D. Ugues [a,b], S. Biamino [a,b], M. Lombardi [a,b], P. Fino [a,b]

[a] Department of Applied Science and Technology, Politecnico Di Torino, Corso Duca degli Abruzzi 24, Torino 10129, Italy
[b] Center of Integrated Additive Manufacturing (IAM), Politecnico di Torino, Corso Castelfidardo, 51, Torino 10138, Italy

ARTICLE INFO

Keywords:
Hot isostatic pressing
Laser powder bed fusion
A205 alloy
Microstructure evolution
Precipitation hardening
Incipient melting

ABSTRACT

Hot isostatic pressing (HIP) is increasingly used as a post-processing technique for components produced via laser powder bed fusion (LPBF). However, the microstructural evolution of the as-HIPed condition, particularly in precipitation-hardening alloys, remains largely unexplored. This study investigates the as-HIPed microstructure of a precipitation-hardening Al-Cu-Mg-Ag-Ti-B (A205) alloy processed by LPBF. A combined HIP & solution treatment (HIP-Quench) was performed in a single-step to evaluate the effectiveness of HIP in promoting the dissolution of secondary phases. The HIP cycle involved a controlled ramp rate (7 °C/min) to the desired solution temperature, a 1-hour hold at 100 MPa, followed by quenching. Solution temperatures of 530 °C and 540 °C were examined. For a comparison, an equivalent non-HIP cycle with various interruptions was conducted. Preliminary assessments revealed a reduction in porosity from 0.23 % in the as-built condition to 0.05 % and 0.07 % in the as-HIPed conditions. Microstructural analysis indicated that, despite HIP-Quench being conducted at different solutioning temperatures, the complete dissolution of the θ-Al_2Cu phase was not achieved. Furthermore, signs of incipient melting along the grain boundaries were noticed in both HIPed samples but were absent in the non-HIPed samples. The findings suggest that HIP treatment induces re-precipitation of the blocky θ-Al_2Cu phase along the grain boundaries, which subsequently undergoes interfacial premelting.

1. Introduction

Laser powder bed fusion (LPBF) is one of the most widely used additive manufacturing (AM) technologies, capable of building 3D parts directly from a CAD file in a layer-by-layer fashion by melting powder particles and a high-energy laser source [1]. Although the technology is highly promising, the number of alloys that can be effectively processed via LPBF remains limited [2]. The A205 alloy (also referred to as A20X™) is a promising high-strength aluminium alloy (Al-Cu-Mg-Ag--Ti-B) explicitly developed for LPBF processing. The alloy is qualified under SAE standards for AM component use in the aerospace industry [3]. Its excellent processability stems from the presence of pre-embedded nano- and micro-sized TiB_2 particles, which significantly reduce hot cracking susceptibility and enhance the absorptivity of the fiber laser [4,5]. The titanium and boron present as alloying elements are responsible for the in-situ formation of TiB_2 particles in molten aluminium, typically produced via a salt-melt method [6,7]. During the LPBF process, these TiB_2 particles act as potent grain refiners by promoting the formation of equiaxed grains, which are effective in suppressing hot cracking. Consequently, as-printed A205 parts are generally free from hot cracks, making the alloy well-suited for LPBF processing [2,5].

Being a precipitation-hardening alloy, considerable attention has been given to post-processing temper treatments such as T6 and T7, which involve solution treatment followed by artificial aging [7,8]. In the T6 or T7 condition, the A205 alloy gains strength by precipitation of nano-sized, plate-like coherent Ω and semi-coherent θ′ phases [8]. Both Ω and θ′ are metastable precipitates that form from a supersaturated solid solution (SSSS) and eventually transform into the equilibrium θ-Al_2Cu phase through the following sequence [8]:

$$\text{SSSS} \rightarrow \text{G.P. Zone (Cu)} \rightarrow \theta'' \rightarrow \theta' \text{ on } \{0\ 0\ 1\}_{Al} \rightarrow \theta$$

---

* Corresponding author.
E-mail addresses: jayant.barode@polito.it (J. Barode), emilio.bassini@polito.it (E. Bassini), alberta.aversa@polito.it (A. Aversa).

https://doi.org/10.1016/j.jallcom.2025.181817
Received 23 April 2025; Received in revised form 14 June 2025; Accepted 23 June 2025

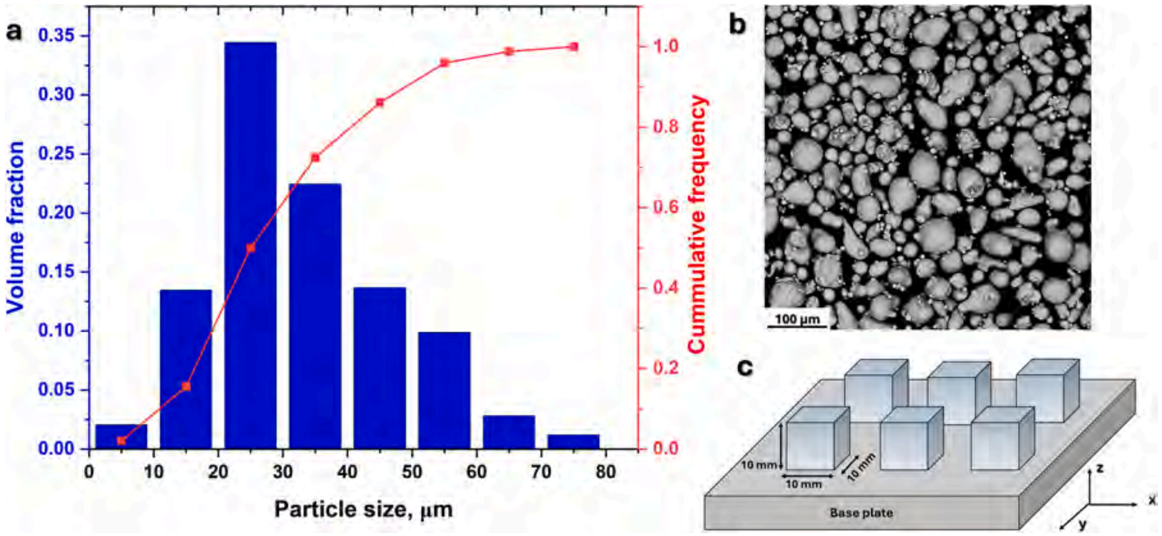

Fig. 1. (a) A205 powder particle size distribution, (b) SEM-SE micrograph showing particle morphology, and (c) a schematic of LBPF printed cuboidal parts.

SSSS → G.P. Zone (Mg and Ag) → Ω on $\{1\ 1\ 1\}_{Al}$ → θ

These precipitates exhibit the following orientation relationships with the Al matrix: $[010]_{\Omega}\ //\ [10\bar{1}]_{Al}$; $(001)_{\Omega}\ //\ (111)_{Al}$ [9], and $(001)_{\theta'} \parallel (001)_{Al}$ and $[100]_{\theta'} \parallel [100]_{Al}$ [10]. The Ω precipitates contribute to a higher strength than θ′ by forming on the {111} planes of Al, which are the primary glide planes in an FCC lattice [11]. The alloy also responds well to the T4 treatment, i.e., a solution treatment followed by natural aging. After T4, the alloy showed improved mechanical properties compared to its as-built condition, particularly in terms of elongation at failure [12].

Despite its good processability by AM, defects such as lack of fusion and gas-induced porosities are inherent in LPBF-processed A205 components [13,14]. These processing-induced defects are also common in other alloys produced by LPBF and have a detrimental effect on the mechanical properties [15,16]. As a result, qualifying such components for safety-critical applications remains a challenge [14]. To mitigate these defects, a post-processing treatment of hot isostatic pressing (HIP) is highly effective [17–20]. Shakil et al. [17] and Koelblin et al. [14] applied HIP treatment to the LPBF-processed A205 alloy, reporting a notable reduction in the porosity fraction. This decrease in porosity significantly enhanced the fatigue life of the component [14]. Four primary mechanisms are responsible for a pore closure through HIP [21,22]: (i) plastic flow, (ii) power-law creep, (iii) Coble creep (grain boundary diffusion), and (iv) Nabarro–Herring creep (lattice diffusion). However, recent studies show conflicting results regarding the effectiveness of HIP on the mechanical properties of LPBF-processed Al alloys. For instance, Ertuğrul et al. found that large internal porosities could be significantly reduced, improving the tensile properties after T6 treatment [23]. In contrast, Hastie et al. [24] and Koelblin et al. [14] reported that HIP treatment could cause pore flattening, resulting in stress concentrations that negatively impact both tensile and fatigue properties. Furthermore, these flattened pores were found to reopen during subsequent post-processing heat treatments [14,25].

Regardless of its effectiveness in closing cracks or pores, HIP treatment inherently alters the microstructure of printed parts [18,26,27]. Liu et al. [27] and Barode et al. [18] observed that the eutectic network of θ-Al_2Cu of the as-built Al-Cu-based alloys produced by LPBF, disintegrated and transformed into coarse or blocky spheroidal θ-Al_2Cu particles after HIP treatment. Similar observations were made for the AlSi10Mg alloy, where the eutectic Si network transformed into coarse Si particles following HIP treatment [26]. Another commonly reported microstructural influence is grain coarsening [19,28]. However, these microstructural effects were observed under conventional HIP treatments, which typically involve slow cooling rates at the end of the cycle [18,29]. Recently, a novel HIP-Quench treatment has been introduced, which enables quenching at rates equivalent to rapid air, water, or oil quenching. HIP-Quench combines HIP and a solution treatment into a single-step [30,31]. This approach can be a game changer for precipitation-hardening alloys, significantly reducing the time and energy required for post-processing.

Table 1
Chemical composition of the A205 alloy powder.

Elements	Al	Cu	Mg	Ag	Ti	B
Nominal value (wt %)	Bal.	4.2–5.0	0.2–0.33	0.60–0.90	3.0–3.8	1.25–1.55
EDS (wt%)	Bal.	4.90	0.20	0.60	3.50	1.30

To date, only a limited number of materials have been studied using HIP-Quench, including Ni-based superalloys [30], 17–4 PH [32], Ti-6Al-4V [33] and AlSi10Mg [34]. However, to the author's knowledge, no study has yet been reported on HIP-Quench treatment of the A205 alloy processed by LPBF. Therefore, in the present work, an attempt has been made to investigate the effect of combined HIP & solution treatment (HIP-Quench) on the as-HIPed microstructure. Two solutioning temperatures (530 °C and 540 °C) were examined. To fully understand the effect of HIP-Quench, a comparison was also made with non-HIPed solution treatments conducted at the same temperature and time specifications as the HIP-Quench cycles. The present experimental findings on the microstructural evolution during HIP-Quench are expected to be crucial for the advancement of this alloy.

2. Experimental

An A205 (Al-Cu-Mg-Ag-Ti-B) powder was purchased from ECKART GmbH. The particle size distribution is shown in Fig. 1**a**, having D_{10}, D_{50} and D_{90} as 12 µm, 25 µm and 49 µm respectively. The powder morphology is presented by SEM-SE micrograph in Fig. 1**b**. The chemical composition of the powder was analyzed using Energy-Dispersive Spectroscopy (EDS) and is presented in Table 1, along with the nominal composition provided by the supplier [35].

Cubic samples with dimensions of $10 \times 10 \times 10\ mm^3$ were printed by LPBF using an EOS M270 dual-mode system under argon atmosphere. The build platform was preheated to 100 °C, and a scanning strategy of

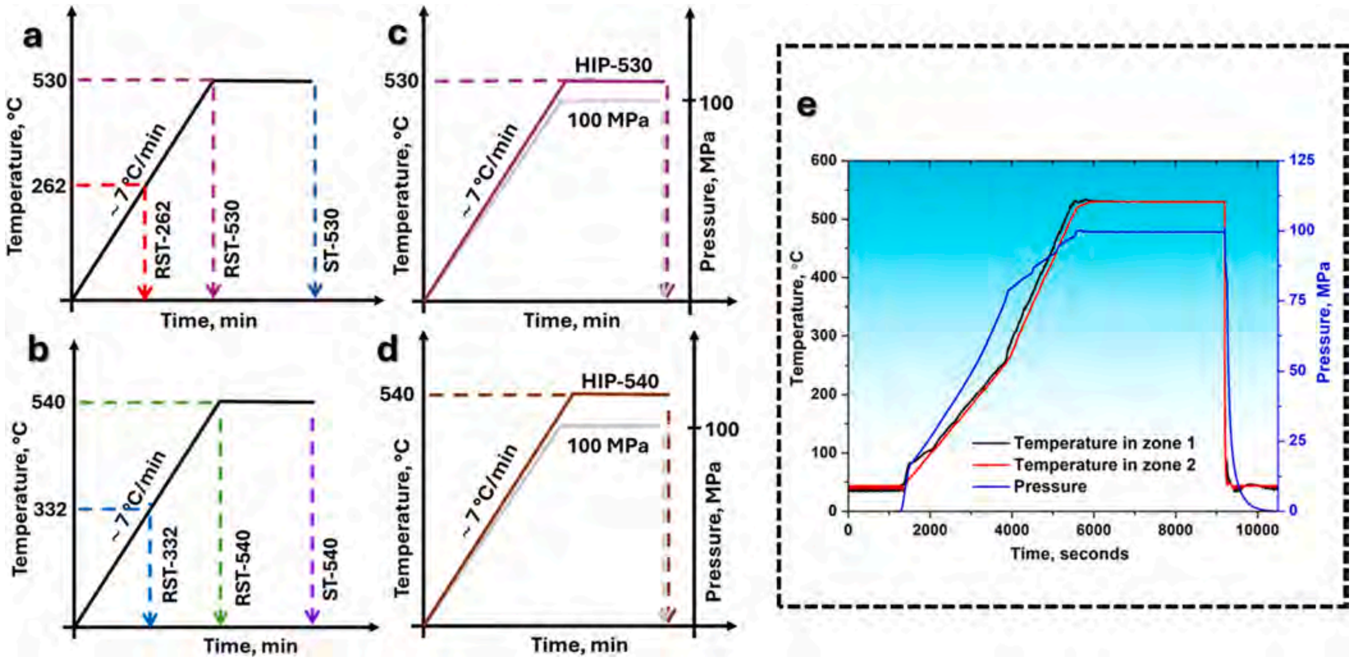

Fig. 2. Graphs showing the heat treatment cycle of HIPed and non-HIPed conditions (a) ST-530, (b) ST-540, (c) HIP-530, (d) HIP-540 and (e) real-time temperature and pressure profile of a HIP-530 cycle.

Table 2
Nomenclature of various heat-treated conditions.

Heat treatment	Temperature, pressure, and time
RST−262	Ramping to 262 °C followed by quenching
RST−332	Ramping to 332 °C followed by quenching
RST−530	Ramping to 530 °C followed by quenching
RST−540	Ramping to 540 °C followed by quenching
ST−530	530 °C for 1 h, followed by quenching
ST−540	540 °C for 1 h followed by quenching
HIP−530	530 °C and 100 MPa for 1 h, followed by URC
HIP−540	530 °C and 100 MPa for 1 h, followed by URC

67° stripe rotation between successive layers was employed. The optimized printing parameters were obtained from our previous work [12]: laser power = 195 W, scan speed = 800 mm/s, hatch distance = 0.13 mm, layer thickness = 30 µm, resulting in a volumetric energy density (VED) of 62.5 J/mm^3 .

HIP-Quench cycles were performed using the uniform rapid cooling (URC) module of a Quintus QIH 15 L machine equipped with a molybdenum furnace. The URC module was calibrated with a precision of ± 1 °C and ± 0.5 MPa. The HIP-Quench cycles consisted of heating in an inert argon atmosphere from room temperature to either 530 °C or 540 °C at a rate of ~7 °C/min, holding for 1 h at the target temperature under 100 MPa pressure, followed by quenching at a rate of ~770 °C/min. As the dissolution temperature of the θ-Al_2Cu phase is around 525–530 °C [8,12], two solution temperatures were selected (530 °C and 540 °C) as they are very close to the dissolution temperature, with one being slightly higher (540 °C) to achieve a more complete dissolution. Various interrupted heat treatments were performed to track the microstructural evolution in the non-HIPed conditions under the same heat treatment cycle as the HIP-Quench ones. The non-HIPed samples were water-quenched at the end of their respective cycles. Fig. 2 illustrates the graphs for the HIPed (Fig. 2**c-d)** and non-HIPed (Fig. 2**a–b)** cycles, including various interrupted conditions. The real-time thermal and pressure profile during the HIP-530 cycle is displayed in Fig. 2**e**. The nomenclature of the various heat-treated conditions is presented in Table 2. Microstructural characterization was performed on the XZ plane, i.e., along the build direction of the HIPed and non-HIPed samples.

Metallographic sample preparation involved grinding with SiC papers up to 4000 grit and final polishing with colloidal silica. Polished samples were examined under a microscope without etching. The microstructure was observed using a Phenom XL tabletop scanning electron microscope (SEM) equipped with secondary electron (SE), backscattered electron (BSE) detectors, and EDS for low-magnification imaging. Higher magnification micrographs were acquired using a TESCAN S900 field emission scanning electron microscope (FESEM) with an In-Beam SE/BSE detector. The thermal behaviour of as-built (AB) samples was assessed by Differential Scanning Calorimetry (DSC), performed using a NETZSCH 214 Polyma. Samples were heated from 25 °C to 570 °C at 20 °C/min in a nitrogen atmosphere. Baseline correction was applied using the NETZSCH Proteus software.

Macro-porosity content was measured from SEM-BSE micrographs at 500x magnification. A minimum of 10 micrographs in each condition were collected and analyzed using ImageJ software. Phase analysis was conducted by X-ray diffraction (XRD) using a Panalytical Empyrean system with monochromatic Cu-Kα radiation ($\lambda = 1.54$ Å), operated at 40 kV and 40 mA, with a step size of 0.013° and a dwell time of 25 s per step.

3. Results

3.1. Macro-porosity before and after HIP-Quench

The low-magnification SEM-BSE micrographs in Fig. 3 displays the macro-porosity content and the corresponding pore size and shape. The macro-porosity was drastically reduced after HIP-Quench, a result consistent with findings in the literature regarding the effect of post-HIP processing on porosity. The total porosity content decreased from 0.23 % in the AB condition to 0.05 % and 0.07 % in the HIP-530 and HIP-540 conditions, respectively. In addition to macro-porosity content, the pore size and shape were also evaluated. Pore shape was assessed using the circularity value (C), defined as below [36].

$$C = 4\pi \frac{Area}{Perimeter^2} \quad (1)$$

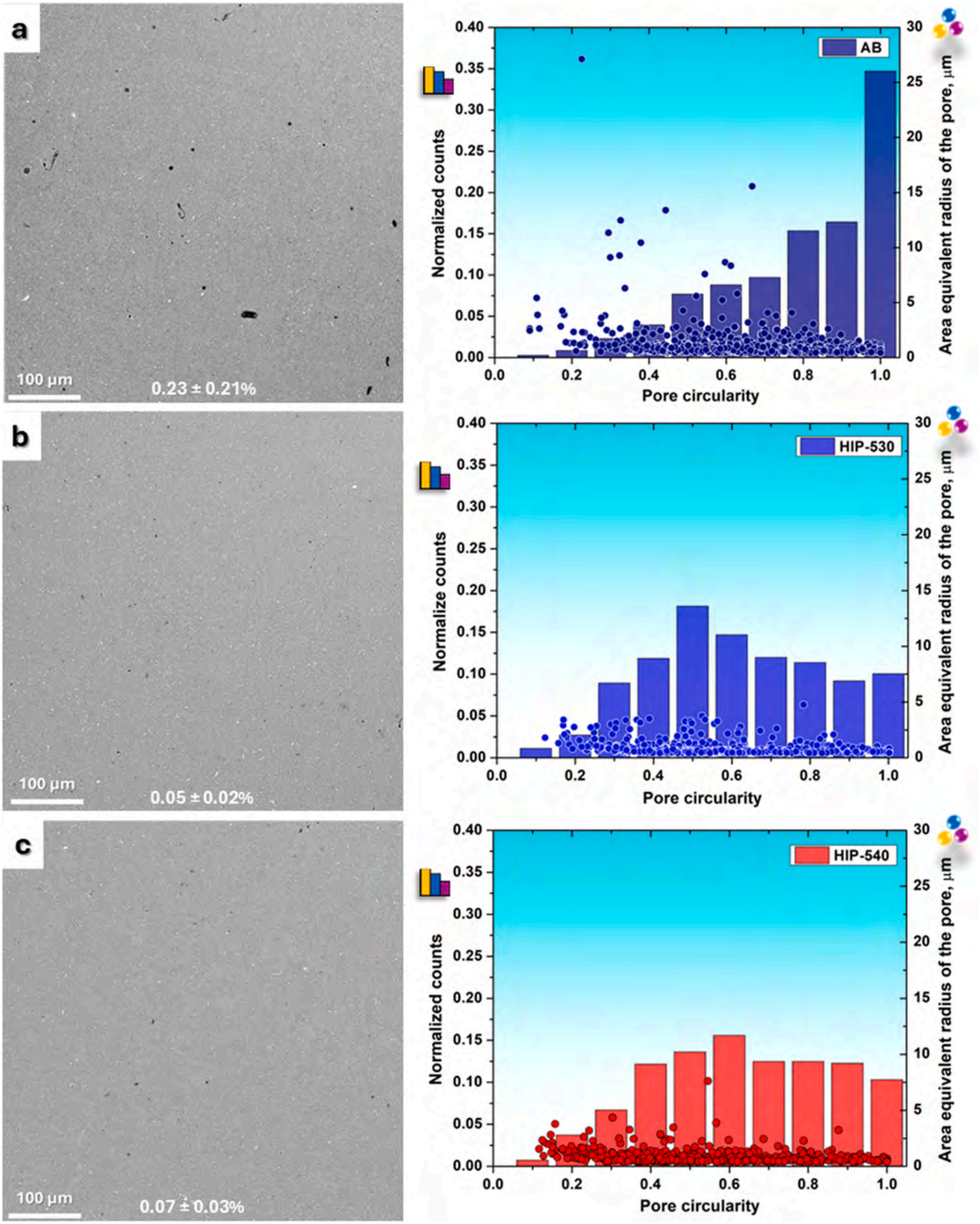

Fig. 3. Low-magnification SEM-BSE micrographs with macro-porosity content in (a) AB, (b) HIP-530 and (c) HIP-540 with their corresponding pore size distribution and circularity.

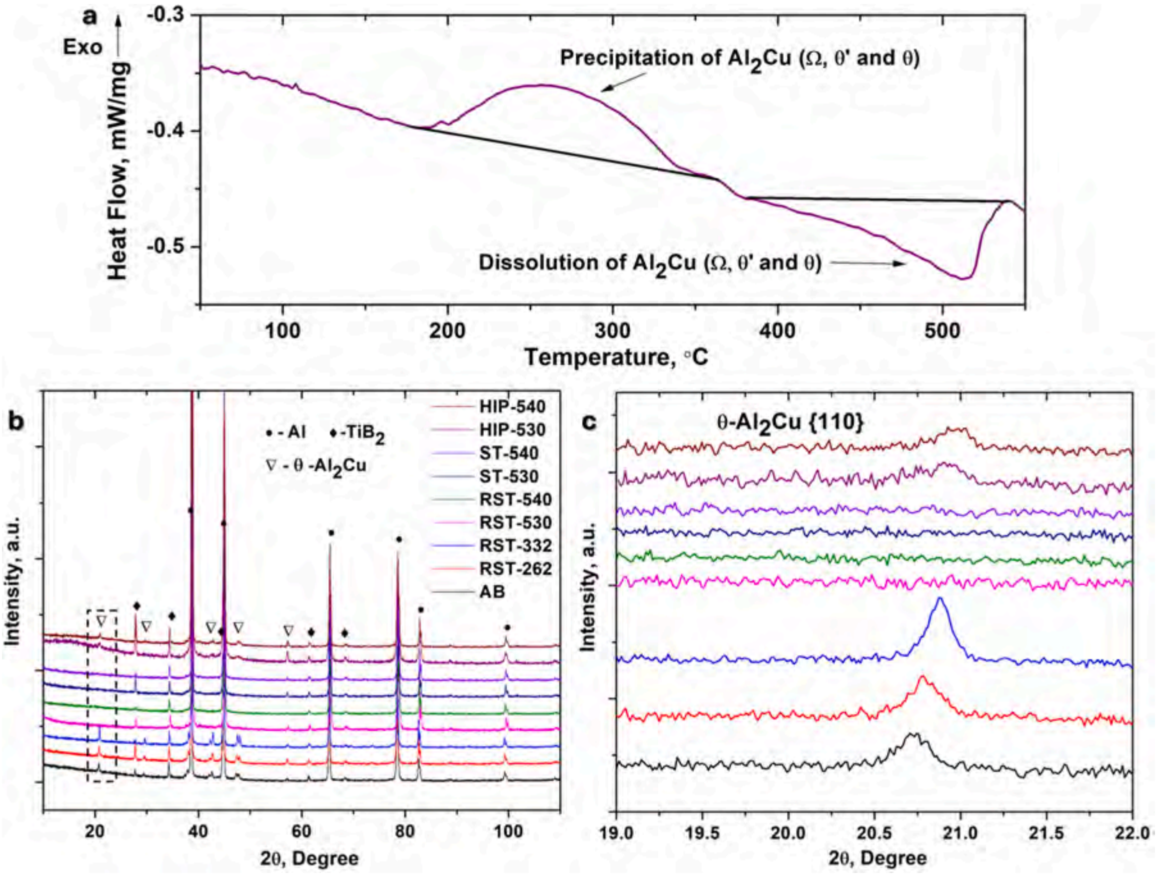

Fig. 4. (a) DSC profile of the AB sample. (b-c) XRD pattern of various conditions of the HIPed and non-HIPed cycles showing (b) whole line profile, and (c) individual peak profile of θ-Al_2Cu {110}.

A circularity value of 1 indicates a perfectly circular pore, while values approaching 0 correspond to non-spherical (irregular) shapes. Pores with $C > 0.75$ are typically considered spherical, as reported elsewhere [37].

A comparison of the circularity and equivalent radius of pores in the AB and HIPed conditions (Fig. 3) revealed that HIP treatment significantly altered the shape and size of the pores. The AB condition contained a high number of fine and circular pores ($C \approx 1$), as seen in Fig. 3**a**. A few larger pores exhibited irregular shapes ($C < 0.75$). Following HIP treatment, the pores became much finer (Fig. 3**b** and Fig. 3**c**), indicating a substantial reduction in their size, especially for the larger and irregular pores. In addition, the average circularity value also decreased to 0.5 and 0.6 for HIP-530 and HIP-540, respectively. This fact implies that although the pores were finer, they were irregular.

3.2. Thermal and phase analysis

The thermal behaviour of the AB obtained by DSC is shown in Fig. 4**a**. A broad exothermic peak ranging from 190 to 330 °C corresponds to the precipitation of various forms of Al_2Cu phases, such as Ω, θ′, and θ [8,12]. A broad endothermic peak ranging from 400 to 530 °C was observed at higher temperatures, representing the dissolution of all forms of Al_2Cu phases. The peak terminates at around 530 °C, corresponding to the dissolution of the coarse/blocky-θ phase.

The phase analysis of the AB, HIPed, and non-HIPed samples is presented in Fig. 4**b** and Fig. 4**c**. The primary identified phases were Al, θ-Al_2Cu, and TiB_2. To evaluate the effectiveness of the combined HIP and solution treatment as a single-step on the θ phase dissolution, the individual θ {110} peak profiles were examined and shown in Fig. 4**c**. The peak intensity decreased from AB to HIP-530 and HIP-540 cycles, although a low intensity of θ peak was noticed in both the HIP conditions, indicating an incomplete dissolution. Interestingly, the θ peak was not detected in samples subjected to the same heat treatment cycle under the ambient pressure i.e., ST-530 and ST-540, suggesting a more complete dissolution in the non-HIPed cycles.

XRD was performed on various interrupted heat treatments to investigate further the dissolution behaviour of the θ phase during the non-HIPed cycles (see Fig. 4**b and c**). At the midpoint of the ramping stages (RST-332 and RST-262), the θ peak intensity increased relative to the AB condition, indicating precipitation of the θ phase. This observation aligns well with the AB condition's DSC profile, showing the precipitation peak from 190 to 330 °C. However, the θ phase dissolved after the ramping stage was completed (RST-530 and RST-540) (Fig. 4**c**).

3.3. Microstructural evolution during non-HIPed cycles

The microstructural evolution during the non-HIPed cycles is presented in Fig. 5. The SEM-BSE micrographs of various interrupted heat treatments are displayed, starting from its AB condition to the solution treatment at 530 °C for 1 h (Fig. 5**a-b-d-f**) and at 540 °C for 1 h (Fig. 5**a-c-e-g**). A similar microstructural evolution was observed in both the solution treatments. The AB microstructure exhibited a network of continuous eutectic-θ along the cell boundaries (Fig. 5**a**). Upon ramping (RST-262 and RST-332), the continuous θ cell boundaries began to fragment and become discontinuous (orange arrows). Further, precipitation of finer θ particles inside the α-Al cells can also be seen (Fig. 5**b-c**). Most of the eutectic-θ dissolved back into the matrix as soon as 530 °C or 540 °C was reached (Fig. 5**d-e**). During the dwell time of 1 h, the dissolution of θ continued (Fig. 5**e-f**). Most of the θ dissolved. However, a few undissolved θ coalesce, become isolated, and form a coarser

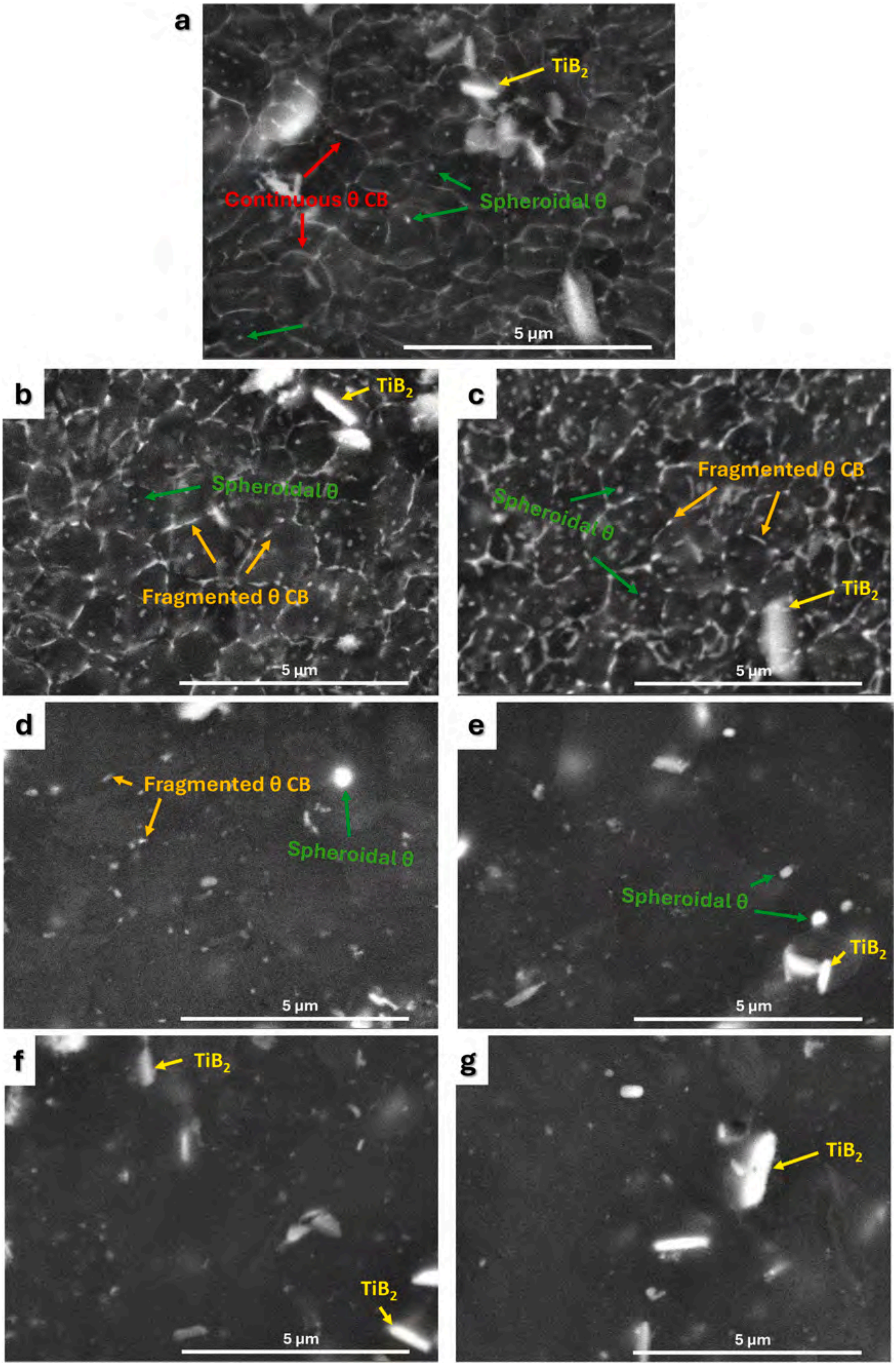

Fig. 5. SEM-BSE micrograph of (a) AB, (b) RST-262, (c) RST-332, (d) RST-530, (e) RST-540, (f) ST-530 and (g) ST-540. *(White arrows indicate TiB_2, green arrows indicate spheroidal θ, yellow arrows indicate the fragmented θ cell boundary, while red arrows indicate the continuous θ cell boundary (CB)).*

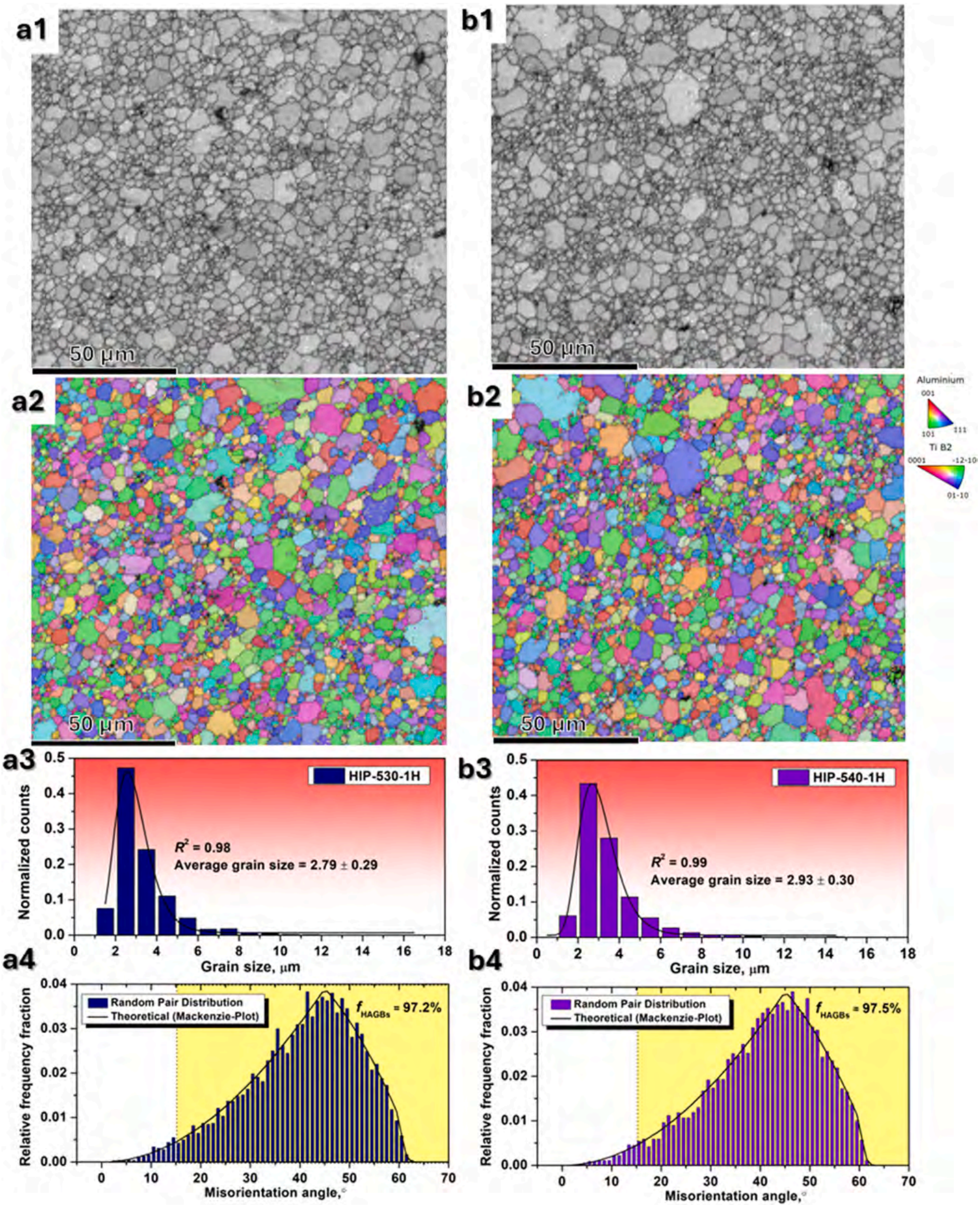

Fig. 6. EBSD micrographs showing (a1-b1) IQ map, (a2-b2) IPF map, (a3-b3) grain size distribution and (a4-b4) boundary misorientation distribution in (a1-a4) HIP-530 and (b1-b4) HIP-540.

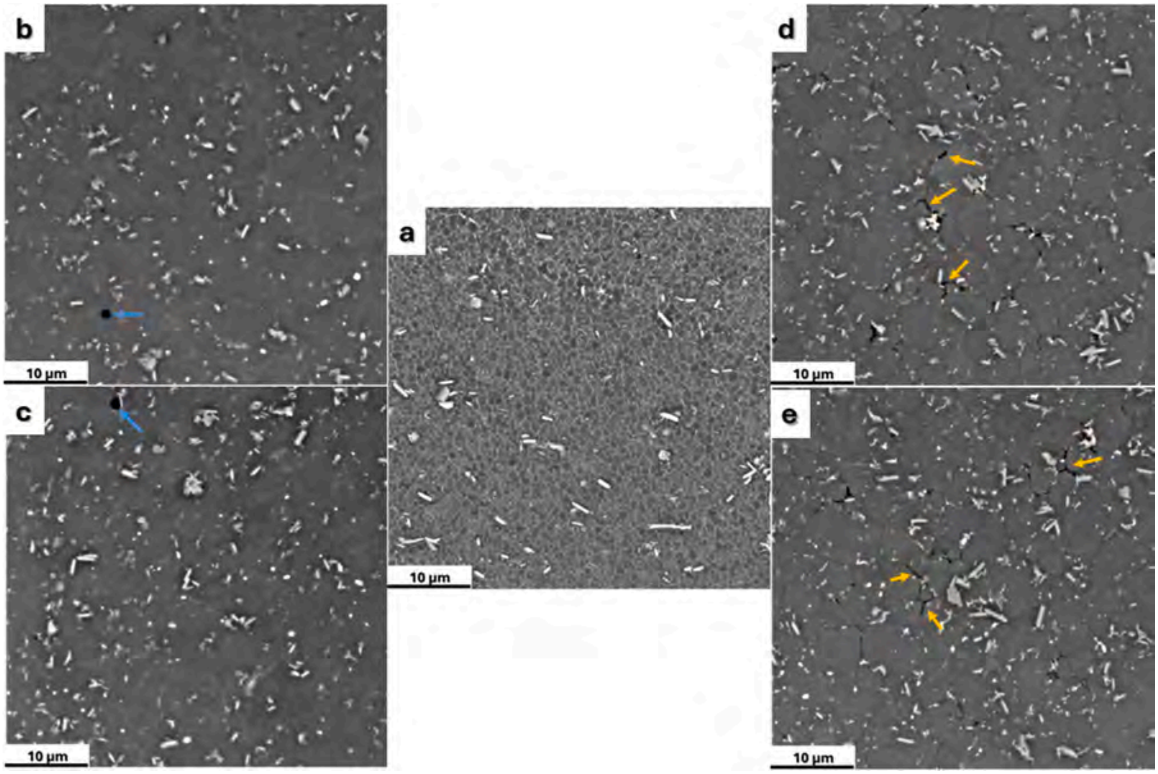

Fig. 7. SEM-BSE micrograph of (a) AB, (b) ST-530, (c) ST-540, (d) HIP-530, and (e) HIP-540. *(Blue and orange arrows indicate spherical and elongated pores, respectively).*

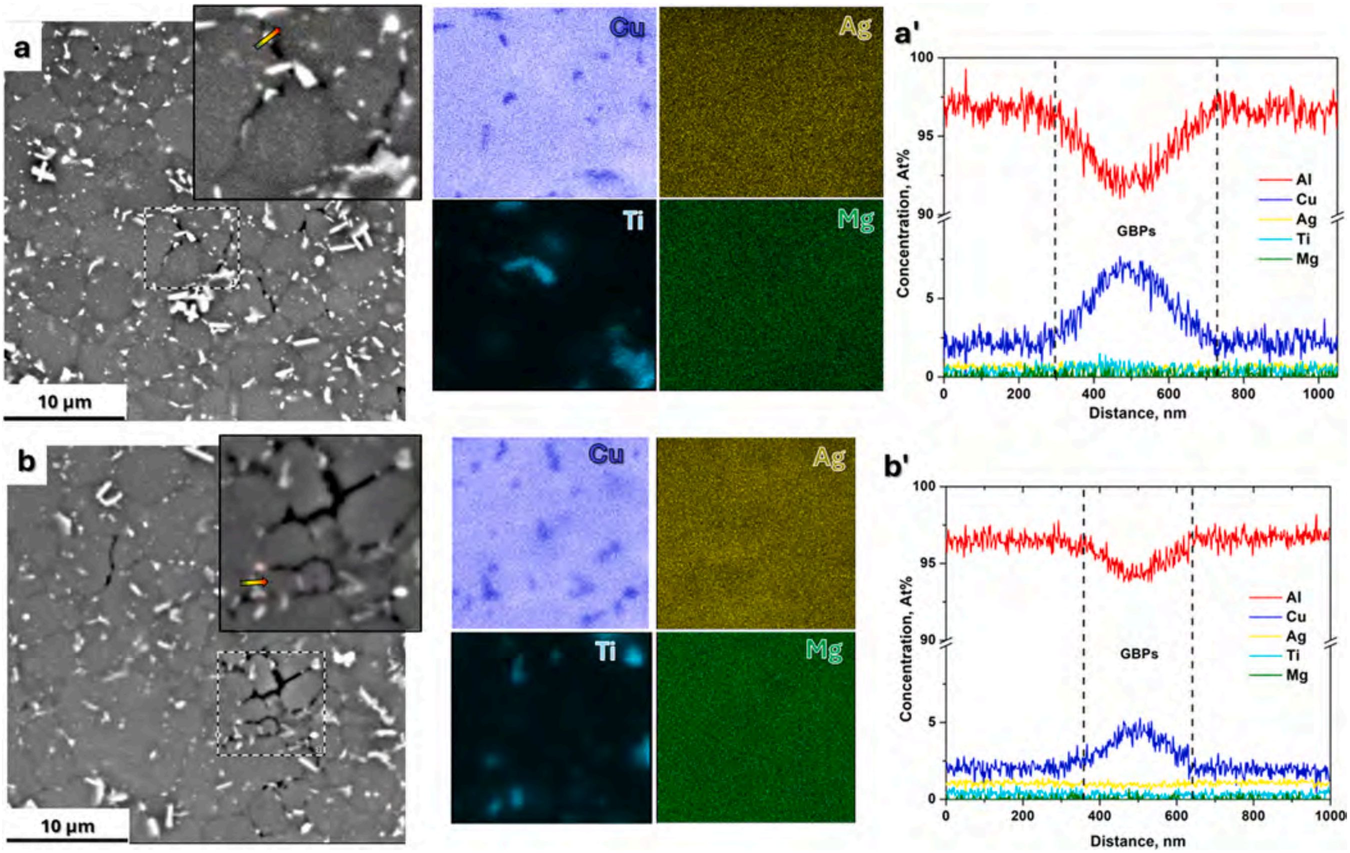

Fig. 8. SEM-BSE micrograph of HIPed LPBF A20X™ alloy showing (a and b) EDS maps on the selected incipient melted region and (a' and b') an elemental line scan across a grain boundary precipitate in (a-a') HIP-530 and (b-b') HIP-540 condition.

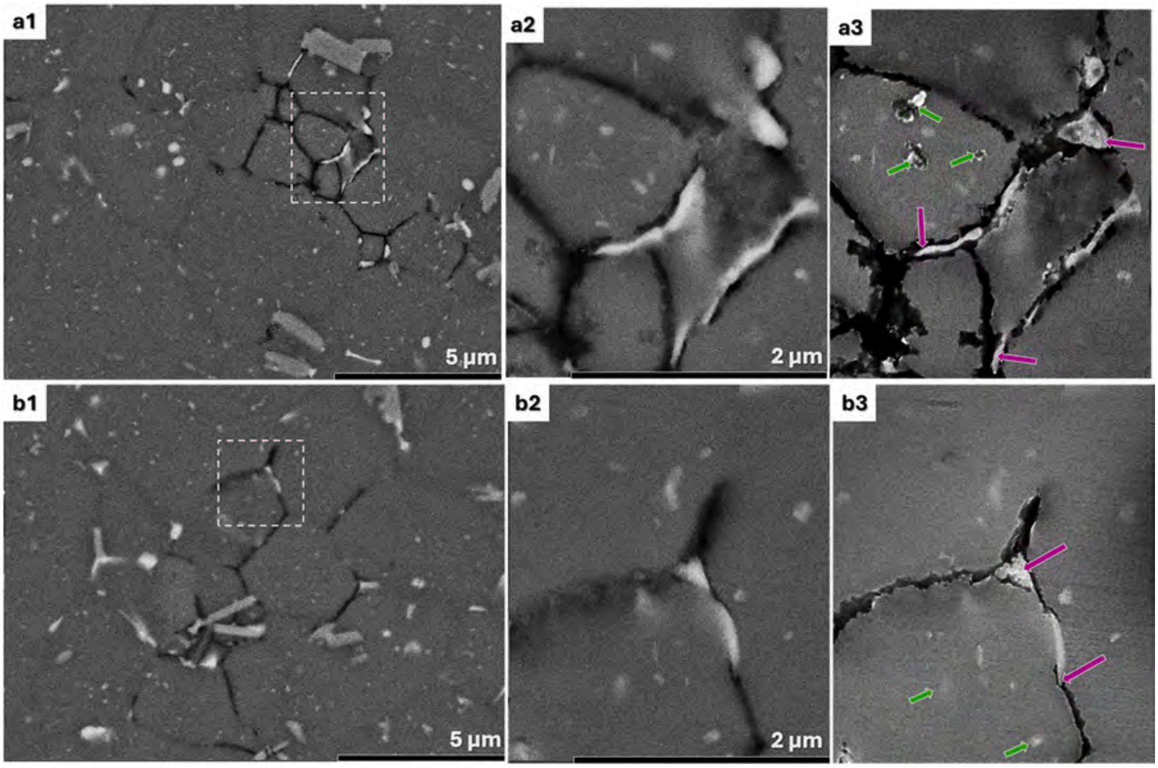

Fig. 9. HR-SEM micrographs of the incipient melted regions in a (a1-a3) HIP-530, and (b1-b3) HIP-540 showing (a1-b1) low magnification BSE, (a2-b2) high magnification BSE micrograph selected region, and (a3-b3) their corresponding SE micrographs *(showing θ-Al_2Cu precipitates inside the grain by green arrows and along grain boundaries by the pink arrow)*.

spheroidal θ phase (indicated by the green arrows).

3.4. Microstructure after HIP-Quench

After the HIP cycle, the microstructure was observed by EBSD (Fig. 6). The analysis extracted image quality (IQ) maps (Fig. 6**a1-b1**), inverse pole figure (IPF) maps **(Fig. 6a2-b2)**, grain size distributions **(Fig. 6a3-b3)**, and the distribution of boundaries as a function of misorientation angle **(Fig. 6a4-b4)** for HIP-530 **(Fig. 6a1-a4)** and HIP-540 **(Fig. 6b1-b4)**, respectively. The microstructural features appeared similar for both HIP-530 and HIP-540. The similarities are listed below:

i. Most grains are fine, ranging between 2 and 4 µm and a few coarser ones.
ii. The grain size distribution follows a Lorentzian curve, with average grain sizes of 2.79 µm and 2.93 µm for HIP-530 and HIP-540, respectively.
iii. No crystallographic texture was observed. This observation was also supported by the distribution of grain boundaries as a function of misorientation angle, as shown by a histogram. The histogram with a distribution peaking at 45° represents a random texture [38].
iv. Nearly 97 % of the boundaries are high-angle grain boundaries (HAGBs).

A somewhat contrasting microstructure was noticed compared to the non-HIPed conditions (AB, ST-530, and ST-540) when observed under the SEM-BSE microscope (Fig. 7). The grain boundaries in HIPed conditions were accompanied by micro-porosities, marked by orange arrows in Fig. 7**d** and Fig. 7**e**. As these were formed along the grain boundaries, they possess an elongated morphology. In contrast, none of the non-HIPed conditions showed grain boundary porosities (Fig. 7**a, b, and c)**. Instead, the gas entrapment likely generated circular porosities (blue arrows in Fig. 7**b** and Fig. 7**c**) during LPBF processing.

In addition to micro-porosities, precipitates were found along the grain boundaries (Fig. 8). Further characterization at higher magnification of the grain boundary region was carried out by performing an SEM-EDS map (Figs. 8**a and** 8**b)** and line scan across these grain boundary precipitates (GBPs) (Fig. 8**a' and 8b')** in both the HIP-530 and HIP-540 conditions, respectively. In both the HIPed conditions, it was observed that the GBPs were rich in Cu, as demonstrated by the elemental line scan. The concentration profiles of other precipitate-forming solutes, such as Ag and Mg, showed no noticeable variation (Fig. 8**a' and 8b')**. This indicates that these GBPs in the HIP-Quench conditions are likely to be of an equilibrium θ phase.

A more detailed microstructural characterization of the grain boundary porosities in the HIP-Quench condition was carried out using HR-SEM with in-lens SE and BSE detectors (Fig. 9). By initially examining the morphology of these porosities, it was suspected that they originated due to incipient melting of a secondary phase and not from de-cohesion/cracking during plastic deformation by creep [39,40]. Porosities generated by de-cohesion have sharp or jagged interfaces that mirror the fracture path [41,42]. In contrast, pores formed by incipient melting occur through localized melting of secondary phases, forming micro-droplets of liquid that propagate into channels such as grain boundaries. As a result, they have wavy or fluid-like interfaces [39,40]. Furthermore, in the case of incipient melting of secondary phases, unmelted particles are typically seen alongside the porosities. The present work's microstructural features of incipient melting were very evident (see **Fig. 9a1-a3** and **Fig. b1-b3**). The elongated grain boundary porosities are accompanied by un-melted residual θ precipitates (Fig. 9**a3 and Fig. 9b3**, pink arrows). The trailing tip of the un-melted θ precipitates can be seen leading into the incipient melted region. Moreover, some of the θ precipitates within the grains have also begun to melt (green arrows in **Fig. 9a3**), although this was observed less frequently.

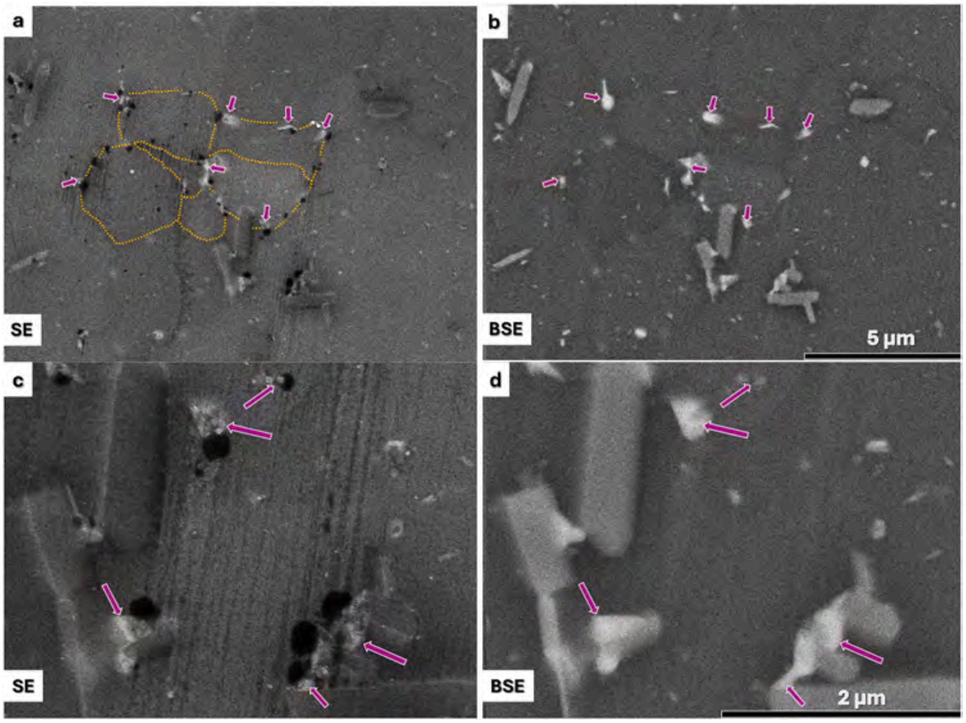

Fig. 10. HR-SEM micrographs of the early formation of incipient melting at the interface of GBPs in a HIP-530 showing SE (left) and corresponding BSE (right) at (a-b) low magnification and (c-d) high magnification *(dotted orange line shows grain boundary, pink arrows show* θ-Al_2Cu *precipitates near micro-pores)*.

At specific locations, an early stage of incipient melting was also observed, as shown in a HIP-530 sample **(**Fig. 10**)**. HR-SEM In-Beam SE and BSE micrographs at low magnification **(**Fig. 10**a and b)** and high magnification **(**Fig. 10**c and d)** revealed discontinuous circular black spots located along the grain boundaries (dotted line). These black spots are preferentially located at the interfaces of Al-matrix and θ precipitates (Fig. 10**c and d**, marked by pink arrows) and resemble the onset of incipient melting. The diameter of these black spots ranged from 100 to 500 nm. However, the corresponding BSE micrographs (Fig. 10**b and d**) do not show these black spots but exhibit the same atomic contrast as the matrix. This could be due to the higher atomic contrast of the θ precipitates and higher sensitivity of the In-Beam SE detector to fine surface details, as opposed to the BSE, whose signals come from a larger depth [43,44].

4. Discussion

4.1. *Macro-porosity size and shape before and after HIP-Quench*

The macro-porosities in the AB state were characterized by many fine and spherical pores ($C = 1$), along with a few large irregular ones ($C = 0.2$–0.6) **(**Fig. 3**a)**. Such a porosity distribution is commonly observed in LPBF parts. The fine and spherical porosities are likely induced by gas entrapment or localized vaporization [25,37]. In contrast, the large irregular porosities could result from a lack of fusion or defects induced by unstable keyhole formation [45]. Trapped gases, such as hydrogen and/or argon, could induce spherical porosities because gas bubbles naturally adopt a spherical shape in a molten liquid to minimize surface energy. Additionally, the rapid solidification during LPBF of the molten liquid prevents the gas from escaping, preserving its spherical form. Hydrogen is known to cause porosities in Al alloys due to its higher solubility in liquid Al than in solid (almost thirty times higher) [37]. Argon could be introduced into the melt either during printing from the chamber atmosphere or as trapped in the gas-atomized powder particles [46]. The irregular porosities result from insufficient time for the molten liquid to fill the existing gaps during the LPBF process [46].

The HIP-Quench treatment considerably reduced the overall porosity content and modified the pore morphology. The average pore circularity values (C) for the HIP-530 and HIP-540 samples fall between 0.5 and 0.6. Such a decrease in circularity following the HIP treatment was also observed in the previous studies [24,37,46]. Hastie et al. [24] observed only a partial closure of small and spherical gas pores, modifying them into a flattened-like morphology following the HIP treatment of LPBF-processed AlSi10Mg alloy. Similarly, Kan et al. [46] also reported the incomplete closure of fine and spherical gas-induced porosities, attributing it to entrapped argon gas. The size and shape of the pores in the present study suggested that, although HIP was effective in reducing the large and irregular porosities, it was not effective in completely closing the fine and spherical porosities induced by gas. The incomplete closure of pores was attributed to entrapped gas (hydrogen/argon) in the pores that were difficult to close. These pores shrank non-homogeneously and thus became non-spherical (irregular) during the HIP treatment [47].

4.2. *Incomplete θ dissolution after HIP-Quench*

Results from XRD **(**Fig. 4**c)** and SEM **(**Fig. 5**)** showed incomplete dissolution of θ after the HIP-Quench treatment (HIP-530 and HIP-540) **(**Fig. 8**)**, whereas a more complete dissolution occurred in the non-HIPed samples (ST-530 and ST-540). Interestingly, even the ramped samples (R-ST-530 and R-ST-540) showed a complete dissolution. Such a distinct observation between the HIPed and non-HIPed samples suggested that the incomplete dissolution of the θ phase in the HIPed samples was likely a result of re-precipitation of the equilibrium θ phase due to diffusional creep. Diffusional creep is one of the creep mechanisms that assists in the densification of the parts during HIP. During HIP of A205 alloy, stress-assisted flow of vacancies to and from grain boundaries promoted the transfer of solute atoms (Cu) towards the grain boundaries through lattice diffusion by Nabarro-Herring creep, as well as along the grain boundaries by Coble creep [48,49]. Depending on the applied stress and temperature, both Nabarro-Herring and Coble creep could dominate during the HIP cycle [21,22].

Among the major solute elements in the A205 alloy, such as Cu, Mg, and Ag, Cu has a higher segregation tendency towards the grain boundaries (GB) at elevated temperatures [50,51]. The higher segregation tendency of Cu and its higher concentration (4–5 wt%) in the A205 alloy likely promoted the precipitation of θ along the GBs. Bhal et al. [52] conducted compressive creep tests on a cast Al-Cu-Mn-Zr alloy at 300 °C with two different Cu concentrations (6Cu and 9Cu). They observed an increase in the volume fraction of θ precipitates along the grain boundaries from 0.7 % in 6Cu to 6 % in 9Cu due to diffusional creep. Furthermore, HIP-induced defects, such as vacancies and dislocations caused by power law or dislocation creep, likely enhanced the mobility of solute atoms towards the grain boundary and accelerated the grain boundary precipitation [21,53–55]. Nasedkina et al. [53] also found that the strain-induced vacancies and dislocations contributed to the enhanced diffusion of Cu atoms towards grain boundaries in an Al-Cu binary alloy. That resulted into the decomposition of solid solution and promoted the precipitation of the equilibrium θ phase along the grain boundaries and triple junctions.

In the present work, the GBs and triple junctions in the HIPed microstructure were accompanied by θ precipitates, see Fig. 4**c** and Fig. 6. These precipitates were of blocky nature, which is a typical characteristic of an equilibrium θ phase in Al-Cu-based alloys [56,57]. In the case of non-HIPed samples (R-ST and ST), during ramping, the continuous eutectic-θ cell boundaries initially broke down into discontinuous ligaments, and then into finer particles (Fig. 5**b-c**). These finer eutectic-θ particles possess faster dissolution characteristics than the blocky-θ particles [57,58]. Han et al. [56] revealed the dissolution behaviour of the eutectic- and blocky-θ phase. The eutectic-θ underwent necking at several points along the length of the ligament, leading to the breaking of longer ligaments into finer fragments. A gradual spheroidization and dissolution occurred by radial diffusion of the Cu atoms into the surrounding Al matrix. In contrast, the blocky-θ did not fragment but dissolved only by spheroidization and radial diffusion, which took a much longer time. Thus, the dissolution of blocky-θ was more difficult than that of eutectic-θ. It was also very evident from the micrographs displaying microstructural evolution (Fig. 5). Most of the θ phase dissolved back into the matrix as soon as the solutioning temperature (RST-530 and RST-540) was reached (Fig. 5**d-e**). Since, in ST and RST conditions, the finer eutectic-θ dissolved rather than the blocky-θ, the dissolution kinetics were faster (Fig. 5).

4.3. *Incipient melting in HIP-Quench*

The HIPed samples (HIP-530 and HIP-540) showed signs of incipient melting of GBPs (Fig. 6), while in non-HIPed conditions, incipient melting was not observed. The EDS line scan across the GBPs showed only Cu segregations, indicating that the GBPs were of θ-Al_2Cu. It was suspected that incipient melting could have been due to the premelting of θ GBPs. Lombardi et al. [39] and Andilab et al. [40] observed incipient melting of the θ phase in-situ by laser scanning confocal microscopy in Al-Cu-based alloys. They noticed that θ GBPs pre-melted due to interfacial premelting [39]. Interfacial premelting is a phenomenon where a thin liquid-like layer forms at the interfaces of a material, such as phase boundaries, grain boundaries, or surfaces, at temperatures slightly below the bulk melting point of a phase. This phenomenon occurs due to the higher energy and atomic disorder at these interfaces, along with compositional gradients and Gibbs-Thomson effects, which lowers the melting temperature locally compared to the bulk material [59].

Interfacial premelting is also highly influenced by the morphology of the θ phase [39]. In the HIPed samples, the θ GBPs exhibited an elongated morphology, which possessed higher interfacial energy between the Al matrix and the θ phase, lowering the energy barrier for the nucleation of liquid. Such a morphology favoured interfacial premelting [39,40]. In contrast, in the non-HIPed samples, the θ phase was isolated and spheroidal in morphology, thereby possessing lower interfacial energy than the elongated one. This could have been the reason for the absence of incipient melting in the non-HIPed samples. Interfacial premelting was visible in Fig. 10, which captured the onset of melting of the blocky-θ GBPs in a HIP-530 sample. The presence of micro-pores, specifically at the interfaces of Al matrix-θ precipitates, indicated the existence of liquid micro-droplets during the HIP cycle, eventually forming micro-pores. Reiso et al. [60] demonstrated that local melting could occur in an Al-4.2 wt% Cu alloy along the grain boundaries even when the bulk Cu composition was lower than the maximum solubility limit. They reported that local compositions could exceed the critical concentration due to segregation, causing the incipient melting. The HIP temperatures (530 °C and 540 °C) examined in the present work were very close to the dissolution temperature of the θ phase (~530 °C), as noted from the DSC profile (Fig. 4**a**), allowing the diffusion of Cu atoms from the θ precipitate to the interface of the θ-Al matrix. This could have increased the Cu concentration at the interface to that of the eutectic concentration [61]. Since the stability of liquid at this Cu concentration was more favourable, micro-droplets of liquid likely formed at the θ-Al interface due to reduced Gibbs free energy [40,60]. Consequently, during the prolonged holding time, the micro-droplets form micro-pores at these interfaces due to the movement of vacancy and their clusters to form pores [39,40]. The occurrence of interfacial premelting at grain boundaries (high-energy regions) could have been further assisted by the presence of additional defects, such as vacancies and dislocations in the vicinity of the grain boundaries [62,63], which were inherently generated during the HIP cycle [21,22].

One possible argument is that the incipient melted phase could have been the eutectic-θ of the AB condition, which had formed due to rapid solidification inherent to the LPBF process. The eutectic-θ was present along the cell boundaries as a continuous network (Fig. 5**a** and Fig. 7**a**). The cell size in the AB state was approximately 1.05 µm, as reported in our previous work [8]. These were significantly smaller than the grain sizes observed in the HIPed state (2.79 µm for HIP-530 and 2.93 µm for HIP-540). Since the incipient melted porosities were found along the grain boundaries of the HIPed samples, it suggested that the eutectic-θ cell network had likely broken down first, dissolved and re-precipitated into the equilibrium blocky-θ phase. This blocky-θ phase appeared to have re-precipitated along the grain boundaries due to the enhanced mobility of solute atoms towards and along the grain boundaries (diffusional creep) during the HIP cycle. The above hypothesis aligned well with our observations in the non-HIPed microstructures, where the eutectic-θ cell network broke down into smaller ligaments upon heat treatment (Fig. 5**b and c**) and subsequently dissolved into the Al matrix (Fig. 5**d–g**). However, the θ precipitates do not form an elongated morphology but coarsen into a spheroidal morphology due to the absence of creep.

Surprisingly, the grain boundary pores were not fully healed during the HIPed cycles despite the signs of incipient melting. Recently, Gheysen et al. [19] and Hu et al. [20] demonstrated the concept of liquid-assisted healing (LAH) during the HIP treatment to heal the pores completely. LAH utilizes the melting of secondary phases to induce a liquid phase that backfills and heals the pores. However, the incomplete healing observed in the HIPed samples could be attributed to LAH requiring a certain critical volume fraction of liquid to act as an effective healing medium. For example, Hu et al. demonstrated LAH by inducing approximately 10 vol% of liquid, while Gheysen et al. utilized 15 vol%. In the present work, the liquid fraction formed due to incipient melting was likely below the critical threshold required to heal the pores fully. A systematic study on LAH in this alloy was planned for future work. Another factor contributing to the incomplete healing could have been the presence of nano- and micro-sized TiB_2 particles at the grain boundaries and near to the θ precipitates (Fig. 8 and Fig. 9). These hard particles likely hindered the fusion at those locations, thereby preventing the pores from closing completely [21,64,65].

A summary of the microstructural evolution observed during HIPed and non-HIPed treatments, starting from the AB microstructure, is

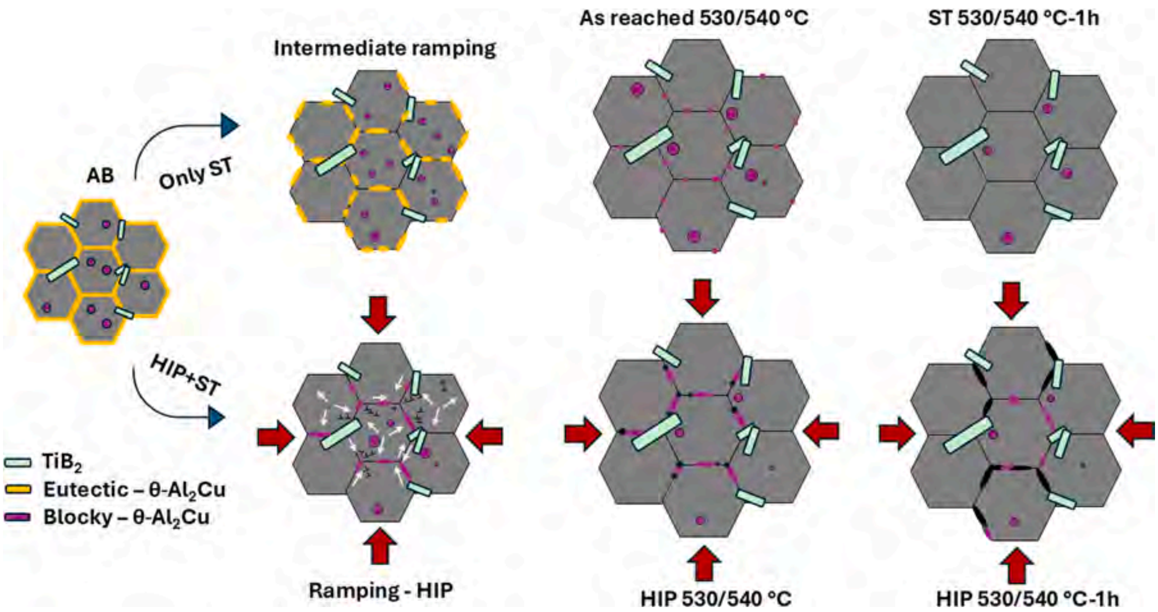

Fig. 11. Schematic of microstructural evolution in a LPBF A205 alloy post treated to a HIP-530/540 cycle and non-HIP-530/540 cycle starting from its as-built state.

presented schematically in Fig. 11. The AB microstructure consists of fine α-Al cells/grains containing few blocky θ-Al$_2$Cu particles. These cells are surrounded by a continuous eutectic-θ network, with elongated nano- and micro- TiB$_2$ particles located at the grain boundaries and triple junctions. During the non-HIP cycle or solution treatment, the eutectic-θ network breaks down into smaller ligaments and dissolves during the ramping stage. The precipitation of blocky-θ also occurs at this stage. Once the solution temperature is reached, most of the eutectic-θ dissolves into the α-Al matrix, leaving a few undissolved, coarser blocky-θ particles within the grains and finer blocky-θ along the grain boundaries. After one hour at the solution temperature, most of the finer blocky-θ dissolves, leaving only the coarser blocky-θ within the grains.

During the HIP cycle, it is believed that the eutectic-θ network of the AB state dissolves and then re-precipitates as blocky-θ along the grain boundaries due to diffusional creep. Once the HIP solution temperature is reached, the elongated blocky-θ precipitates starts to melt due to incipient melting, while some coarser blocky-θ forms within the grains. After one hour of holding time, the incipient melting of the elongated blocky-θ precipitates continues, with only a few coarser blocky-θ remaining undissolved.

5. Conclusions

This study investigated the effect of a combined HIP & solution treatment (HIP-Quench) on the LPBF-processed A205 (A20X™) alloy. Two solution temperatures, 530 °C (HIP-530) and 540 °C (HIP-540), were examined, and the results were compared with non-HIP cycles involving only a solution treatment under identical conditions. The key findings of this work are summarized as follows:

- The HIP treatment effectively reduced macro-porosity in the as-built components, lowering the porosity content from 0.23 % in the as-built state to 0.05 % and 0.07 % in the HIP-530 and HIP-540, respectively.
- The average pore circularity decreased from nearly 1 in the as-built condition to ∼ 0.5–0.6 after the HIP-Quench. This reduction in circularity is attributed to the difficulty in fully closing fine and spherical gas-induced porosities.
- The HIP-530 and HIP-540 exhibited similar microstructural characteristics, including grain size, texture, low- and high-angle grain boundary fractions, incomplete dissolution, and incipient melting of the θ phase.
- Incomplete dissolution of the θ phase was observed after the HIP-Quench, whereas a more complete dissolution occurred in the non-HIP cycle. During the non-HIP cycle, the eutectic-θ network fragmented into smaller particles, thus accelerating dissolution. In contrast, during the HIP cycle, the blocky-θ re-precipitated along the grain boundaries due to diffusional creep. Since the blocky-θ has a slower dissolution rate than the eutectic-θ, the HIP cycles resulted in an incomplete θ dissolution.
- The HIP-Quench microstructure also exhibited signs of incipient melting, primarily along the grain boundaries. This incipient melting was attributed to the interfacial premelting of elongated blocky-θ precipitates present along the high energy regions such as grain boundaries.

HIP remains a highly promising post-heat treatment for high-end LPBF components despite these challenges. However, this study highlights the potential contradictions of HIP when applied in conjunction with exotic heat treatments such as combined HIP & solution treatment. Incipient melting during HIP is not limited to high-strength A20X™ alloy but may also apply to other precipitation-hardening alloys processed by LPBF.

CRediT authorship contribution statement

J. Barode: Writing – original draft. **E. Bassini:** Writing – review & editing. **A. Aversa:** Conceptualization, Writing – review & editing. **F. D'Isanto:** Conceptualization, Writing – review & editing. **D. Ugues:** Supervision. **S. Biamino:** Supervision. **P. Fino:** Supervision.

Declaration of Competing Interest

The authors declare that they have no known competing financial interests or personal relationships that could have appeared to influence the work reported in this paper

Acknowledgements

The study was carried out within the MOST – Sustainable Mobility National Research Center and received funding from the European

Union Next-GenerationEU (Piano nazionale di ripresa e resilienza (PNRR) – missione 4 componente 2, investimento 1.4 – D.D. 1033 17/06/2022, CN00000023). This manuscript reflects only the authors' views and opinions, neither the European Union nor the European Commission can be considered responsible for them.

References

[1] W.E. King, A.T. Anderson, R.M. Ferencz, N.E. Hodge, C. Kamath, S.A. Khairallah, A. M. Rubenchik, Laser powder bed fusion additive manufacturing of metals; physics, computational, and materials challenges, Appl. Phys. Rev. 2 (2015), https://doi.org/10.1063/1.4937809.

[2] J.H. Martin, B.D. Yahata, J.M. Hundley, J.A. Mayer, T.A. Schaedler, T.M. Pollock, 3D printing of high-strength aluminium alloys, Nature 549 (2017) 365–369, https://doi.org/10.1038/nature23894.

[3] SAE International, AMS AM Additive Manufacturing Metals, Aluminum Alloy Powder 4.6Cu - 3.4Ti - 1.4B - 0.75Ag - 0.27Mg, SAE International, 2021, n.d. https://doi.org/https://doi.org/10.4271/AMS7033.

[4] S.A. Butler, An aluminium-copper alloy, GB2334966A, UK Pat. (2003).

[5] P. Mair, L. Kaserer, J. Braun, N. Weinberger, I. Letofsky-Papst, G. Leichtfried, Microstructure and mechanical properties of a TiB2-modified Al–Cu alloy processed by laser powder-bed fusion, Mater. Sci. Eng. A 799 (2021) 140209, https://doi.org/10.1016/j.msea.2020.140209.

[6] M. Indriyati, Effect of TiB2 addition on the microstructure and mechanical properties of Al-Cu-Mg-Ag alloy, Univ. Warwick (2016).

[7] F. Jiang, L. Tang, S. Li, H. Ye, M.M. Attallah, Z. Yang, Achieving strength-ductility balance in a laser powder bed fusion fabricated TiB2/Al–Cu-Mg-Ag alloy, J. Alloy. Compd. 945 (2023) 169311, https://doi.org/10.1016/j.jallcom.2023.169311.

[8] J. Barode, A. Vayyala, E. Virgillito, A. Aversa, J. Mayer, P. Fino, M. Lombardi, Revisiting heat treatments for additive manufactured parts: a case study of A20X alloy, Mater. Des. 225 (2023) 111566, https://doi.org/10.1016/j.matdes.2022.111566.

[9] S.L. Yang, X.J. Zhao, H.W. Chen, N. Wilson, J.F. Nie, Atomic structure and evolution of a precursor phase of Ω precipitate in an Al-Cu-Mg-Ag alloy, Acta Mater. 225 (2022) 117538, https://doi.org/10.1016/j.actamat.2021.117538.

[10] H. Liao, H. Kimizuka, H. Miyoshi, S. Ogata, Origin of the nucleation preference of coherent and semicoherent nanoprecipitates in Al–Cu alloys based on atomistically informed classical nucleation theory, J. Alloy. Compd. 938 (2023) 168559, https://doi.org/10.1016/j.jallcom.2022.168559.

[11] J.F. Nie, B.C. Muddle, Microstructural design of high-strength aluminum alloys, J. Phase Equilibria 19 (1998) 543–551, https://doi.org/10.1361/105497198770341734.

[12] J. Barode, A. Vayyala, A. Aversa, L. Yang, J. Mayer, P. Fino, M. Lombardi, Natural and artificial aging behaviour of Al-Cu-Mg-Ag-Ti-B (A205) alloy processed by laser powder bed fusion: Strengthening mechanisms and failure analysis, Mater. Today Commun. 39 (2024) 108978, https://doi.org/10.1016/j.mtcomm.2024.108978.

[13] M. Ghasri-Khouzani, H. Karimialavijeh, M. Pröbstle, R. Batmaz, W. Muhammad, A. Chakraborty, T.D. Sabiston, J.-P. Harvey, É. Martin, Processability and characterization of A20X aluminum alloy fabricated by laser powder bed fusion, Mater. Today Commun. 35 (2023) 105555, https://doi.org/10.1016/j.mtcomm.2023.105555.

[14] J. Koelblin, N. Cruchley, J. Chamberlin, M.A. Siddiq, D.M. Mulvihill, M.E. Kartal, The influence of post-thermal treatments on microstructure and mechanical properties in A20X alloy fabricated through powder bed fusion, J. Manuf. Process 125 (2024) 93–110, https://doi.org/10.1016/j.jmapro.2024.07.019.

[15] A. Du Plessis, I. Yadroitsava, I. Yadroitsev, Effects of defects on mechanical properties in metal additive manufacturing: A review focusing on X-ray tomography insights, Mater. Des. 187 (2020) 108385.

[16] M.C. Brennan, J.S. Keist, T.A. Palmer, Defects in metal additive manufacturing processes, (2021).

[17] S.I. Shakil, C. Beamer, M.M. Attallah, M. Haghshenas, The effect of heat treatment on local mechanical properties of laser powder bed fused and hot isostatically pressed Al-Cu-Mg-Ag-TiB2 (A20X) aluminum alloy, JOM 76 (2024) 31–41, https://doi.org/10.1007/s11837-023-06233-3.

[18] J. Barode, E. Bassini, A. Aversa, D. Manfredi, D. Ugues, S. Biamino, M. Lombardi, P. Fino, Effect of hot isostatic pressing on the microstructure of laser powder bed fused A20X™ alloy. IOP Conf. Ser. Mater. Sci. Eng., IOP Publishing, 2024, p. 12026, https://doi.org/10.1088/1757-899X/1310/1/012026.

[19] J. Gheysen, D. Tingaud, J. Villanova, A. Hocini, A. Simar, Exceptional fatigue life and ductility of new liquid healing hot isostatic pressing especially tailored for additive manufactured aluminum alloys, Scr. Mater. 233 (2023) 115512, https://doi.org/10.1016/j.scriptamat.2023.115512.

[20] X. Hu, C. Guo, Y. Huang, Z. Xu, Z. Shi, F. Zhou, G. Li, Liquid-induced healing of cracks in nickel-based superalloy fabricated by laser powder bed fusion, Acta Mater. 267 (2024), https://doi.org/10.1016/j.actamat.2024.119731.

[21] H.V. Atkinson, S. Davies, Fundamental aspects of hot isostatic pressing: an overview, Metall. Mater. Trans. A 31 (2000) 2981–3000.

[22] I. Radomir, Densification mechanisms made during creep techniques applied to the hot isostatic pressing 62 (2012) 779–782, https://doi.org/10.1016/j.sbspro.2012.09.131.

[23] O. Ertuğrul, Z.Ç. Öter, M.S. Yılmaz, E. Şahin, M. Coşkun, G. Tarakçı, E. Koç, Effect of HIP process and subsequent heat treatment on microstructure and mechanical properties of direct metal laser sintered AlSi10Mg alloy, Rapid Prototyp. J. 26 (2020) 1421–1434, https://doi.org/10.1108/RPJ-07-2019-0180.

[24] J.C. Hastie, M.E. Kartal, L.N. Carter, M.M. Attallah, D.M. Mulvihill, Classifying shape of internal pores within AlSi10Mg alloy manufactured by laser powder bed fusion using 3D X-ray micro computed tomography: Influence of processing parameters and heat treatment, Mater. Charact. 163 (2020) 110225, https://doi.org/10.1016/j.matchar.2020.110225.

[25] J.C. Hastie, J. Koelblin, M.E. Kartal, M.M. Attallah, R. Martinez, Evolution of internal pores within AlSi10Mg manufactured by laser powder bed fusion under tension: As-built and heat treated conditions, Mater. Des. 204 (2021) 109645, https://doi.org/10.1016/j.matdes.2021.109645.

[26] J.G. Santos Macías, L. Zhao, D. Tingaud, B. Bacroix, G. Pyka, C. van der Rest, L. Ryelandt, A. Simar, Hot isostatic pressing of laser powder bed fusion AlSi10Mg: parameter identification and mechanical properties, J. Mater. Sci. 57 (2022) 9726–9740, https://doi.org/10.1007/s10853-022-07027-9.

[27] X. Liu, Y. Liu, Z. Zhou, H. Zhong, Q. Zhan, A combination strategy for additive manufacturing of AA2024 high-strength aluminium alloys fabricated by laser powder bed fusion: Role of hot isostatic pressing, Mater. Sci. Eng. A 850 (2022) 143597, https://doi.org/10.1016/j.msea.2022.143597.

[28] E. Bassini, A. Sivo, P.A. Martelli, E. Rajczak, G. Marchese, F. Calignano, S. Biamino, D. Ugues, Effects of the solution and first aging treatment applied to as-built and post-HIP CM247 produced via laser powder bed fusion (LPBF), J. Alloy. Compd. 905 (2022) 164213, https://doi.org/10.1016/j.jallcom.2022.164213.

[29] G. Marchese, E. Bassini, A. Aversa, M. Lombardi, D. Ugues, P. Fino, S. Biamino, Microstructural Evolution of Post-Processed Hastelloy X Alloy Fabricated by Laser Powder Bed Fusion, (2019). https://doi.org/10.3390/ma12030486.

[30] L.M. Roncery, I. Lopez-Galilea, B. Ruttert, S. Huth, W. Theisen, Influence of temperature, pressure, and cooling rate during hot isostatic pressing on the microstructure of an SX Ni-base superalloy, Mater. Des. 97 (2016) 544–552, https://doi.org/10.1016/j.matdes.2016.02.051.

[31] C. Beamer, D. Denlinger, S. Rao, C. Dinh, High Pressure Heat Treatment for L-PBF Hastelloy X, in: HT2021, ASM International, 2021, pp. 44–50.

[32] M. Ahlfors, High pressure heat treatment of AM parts - Combining HIP and heat treatment, 30th ASM Heat Treat. Soc. Conf. Expo. Heat Treat 2019 - Ext. Abstr. 2 (2019) 11–17. https://doi.org/10.31399/asm.cp.ht2019p0011.

[33] J. Benzing, N. Hrabe, T. Quinn, R. White, R. Rentz, M. Ahlfors, Hot isostatic pressing (HIP) to achieve isotropic microstructure and retain as-built strength in an additive manufacturing titanium alloy (Ti-6Al-4V), Mater. Lett. 257 (2019) 126690, https://doi.org/10.1016/j.matlet.2019.126690.

[34] M. Tocci, A. Pola, M. Gelfi, G.M. La Vecchia, Effect of a New High-Pressure Heat Treatment on Additively Manufactured AlSi10Mg Alloy, Metall. Mater. Trans. A Phys. Metall. Mater. Sci. 51 (2020) 4799–4811, https://doi.org/10.1007/s11661-020-05905-y.

[35] Eckart GmbH, Technical Information Sheet - A205 gas atomized powder, (n.d.). ⟨https://eckart.net/de/en/microsite/am⟩.

[36] J. Barode, U. Aravind, S. Bhogi, B. Muduli, M. Mukherjee, Mg and mg-based blowing agents for aluminum foam, Metall. Mater. Trans. B 52 (2021) 292–304, https://doi.org/10.1007/s11663-020-02008-2.

[37] N. Mclean, M.J. Bermingham, P. Colegrove, A. Sales, N. Soro, C.H. Ng, M. S. Dargusch, Effect of Hot Isostatic Pressing and heat treatments on porosity of Wire Arc Additive Manufactured Al 2319, J. Mater. Process. Technol. 310 (2022), https://doi.org/10.1016/j.jmatprotec.2022.117769.

[38] D.S. Chezganov, M.A. Borovykh, O.A. Chikova, Prediction of steel corrosion resistance based on EBSD-data analysis, IOP Conf. Ser. Mater. Sci. Eng. 192 (2017) 12031, https://doi.org/10.1088/1757-899X/192/1/012031.

[39] A. Lombardi, W. Mu, C. Ravindran, N. Dogan, M. Barati, Influence of Al2Cu morphology on the incipient melting characteristics in B206 Al alloy, J. Alloy. Compd. 747 (2018) 131–139, https://doi.org/10.1016/j.jallcom.2018.02.329.

[40] B. Andilab, C. Ravindran, N. Dogan, A. Lombardi, G. Byczynski, In-situ analysis of incipient melting of Al2Cu in a novel high strength Al-Cu casting alloy using laser scanning confocal microscopy, Mater. Charact. 159 (2020) 110064, https://doi.org/10.1016/j.matchar.2019.110064.

[41] K. Sadananda, A.K. Vasudevan, N. Phan, Analysis of endurance limits under very high cycle fatigue using a unified damage approach, Int. J. Fatigue 29 (2007) 2060–2071, https://doi.org/10.1016/j.ijfatigue.2007.02.028.

[42] V. Kerlins, Modes of fracture, in: Fractography, Vol 12, By ASM Handb. Committee, ASM Int., 1987: p. p 12–71.

[43] M. Cantoni, L. Holzer, Advances in 3D focused ion beam tomography, MRS Bull. 39 (2014) 354–360, https://doi.org/10.1557/mrs.2014.54.

[44] U. Gernert, D. Berger, Depth Resolution and Surface Sensitivity with the Multiple Detection System of a HR-SEM, Eur. Microsc. Congr. 2016 Proc. (2016) 392–393.

[45] D. Wang, H. Han, B. Sa, K. Li, J. Yan, J. Zhang, J. Liu, Z. He, N. Wang, M. Yan, A review and a statistical analysis of porosity in metals additively manufactured by laser powder bed fusion, OptoElectron Adv. 5 (2022) 210058–210061, https://doi.org/10.29026/oea.2022.210058.

[46] W.H. Kan, Y. Nadot, M. Foley, L. Ridosz, G. Proust, J.M. Cairney, Factors that affect the properties of additively-manufactured AlSi10Mg: Porosity versus microstructure, Addit. Manuf. 29 (2019) 100805, https://doi.org/10.1016/j.addma.2019.100805.

[47] M.R.G. Prasad, S. Gao, N. Vajragupta, A. Hartmaier, Influence of trapped gas on pore healing under hot isostatic pressing in nickel-base superalloys, Crystals 10 (2020) 1147, https://doi.org/10.3390/cryst10121147.

[48] E.D. Hondros, P.J. Henderson, Role of grain boundary segregation in diffusional creep, Metall. Trans. A 14 (1983) 521–530, https://doi.org/10.1007/BF02643770.

[49] S. Shousha, S.B. Kadambi, B. Beeler, B. Kombaiah, Vacancy-mediated transport and segregation tendencies of solutes in fcc nickel under diffusional creep: A density functional theory study, Phys. Rev. Mater. 8 (2024) 1–35, https://doi.org/10.1103/PhysRevMaterials.8.083605.

[50] X.Y. Liu, Q.L. Pan, X. Fan, Y.Bin He, W.Bin Li, W.J. Liang, Microstructural evolution of Al-Cu-Mg-Ag alloy during homogenization, J. Alloy. Compd. 484 (2009) 790–794, https://doi.org/10.1016/j.jallcom.2009.05.046.

[51] B. Zhang, S. Zhang, H. Du, Z. Yao, X. shan Kong, X. Tao, Dependence of Creep Properties on Aging Treatment in Al–Cu–Mg Alloy, Adv. Eng. Mater. 24 (2022) 1–12, https://doi.org/10.1002/adem.202101293.

[52] S. Bahl, J.U. Rakhmonov, C. Kenel, D.C. Dunand, A. Shyam, Effect of grain-boundary θ-Al2Cu precipitates on tensile and compressive creep properties of cast Al–Cu–Mn–Zr alloys, Mater. Sci. Eng. A 840 (2022) 142946, https://doi.org/10.1016/j.msea.2022.142946.

[53] Y. Nasedkina, X. Sauvage, E.V. Bobruk, M.Y. Murashkin, R.Z. Valiev, N.A. Enikeev, Mechanisms of precipitation induced by large strains in the Al-Cu system, J. Alloy. Compd. 710 (2017) 736–747, https://doi.org/10.1016/j.jallcom.2017.03.312.

[54] M. Militzer, W.P. Sun, J.J. Jonas, Modelling the effect of deformation-induced vacancies on segregation and precipitation, Acta Metall. Mater. 42 (1994) 133–141, https://doi.org/10.1016/0956-7151(94)90056-6.

[55] M.E. Kassner, M.-T. Pérez-Prado, Five-Power-Law Creep, 2004. https://doi.org/10.1016/b978-008043637-1/50003-x.

[56] Y.M. Han, A.M. Samuel, F.H. Samuel, H.W. Doty, Dissolution of Al2Cu phase in non-modified and Sr modified 319 type alloys, Int. J. Cast. Met. Res. 21 (2008) 387–393, https://doi.org/10.1179/136404608X347662.

[57] A.M. Samuel, J. Gauthier, F.H. Samuel, Microstructural aspects of the dissolution and melting of Al2Cu phase in Al-Si alloys during solution heat treatment, Metall. Mater. Trans. A 27 (1996) 1785–1798, https://doi.org/10.1007/BF02651928.

[58] E. Sjölander, S. Seifeddine, Optimization of solution treatment of cast Al-7Si-0.3 Mg and Al-8Si-3Cu-0.5 Mg alloys, Metall. Mater. Trans. A 45 (2014) 1916–1927, https://doi.org/10.1007/s11661-013-2141-9.

[59] J.S. Wettlaufer, M.G. Worster, Premelting dynamics, Annu. Rev. Fluid Mech. 38 (2006) 427–452, https://doi.org/10.1146/annurev.fluid.37.061903.175758.

[60] O. Reiso, H.G. Øverlie, N. Ryum, Dissolution and melting of secondary Al2Cu phase particles in an AlCu alloy, Metall. Trans. A 21 (1990) 1689–1695, https://doi.org/10.1007/BF02672585.

[61] G.M. Karthik, G.D. Janaki Ram, R.S. Kottada, Heat-affected zone liquation cracking resistance of friction stir processed aluminum-copper alloy AA 2219, Metall. Mater. Trans. B Process. Metall. Mater. Process. Sci. 48 (2017) 1158–1173, https://doi.org/10.1007/s11663-016-0892-6.

[62] J. Mellenthin, A. Karma, M. Plapp, Phase-field crystal study of grain-boundary premelting, Phys. Rev. B Condens. Matter Mater. Phys. 78 (2008) 1–22, https://doi.org/10.1103/PhysRevB.78.184110.

[63] J. Berry, K.R. Elder, M. Grant, Melting at dislocations and grain boundaries: a phase field crystal study, Phys. Rev. B Condens. Matter Mater. Phys. 77 (2008) 3–6, https://doi.org/10.1103/PhysRevB.77.224114.

[64] H.V. Atkinson, A. Zulfia, A. Lima Filho, H. Jones, S. King, Hot isostatic processing of metal matrix composites, Mater. Des. 18 (1997) 243–245, https://doi.org/10.1016/s0261-3069(97)00058-7.

[65] S.C. Tjong, K.C. Lau, Properties and abrasive wear of TiB2/Al-4%Cu composites produced by hot isostatic pressing, Compos. Sci. Technol. 59 (1999) 2005–2013, https://doi.org/10.1016/S0266-3538(99)00056-1.